Optimization of the Bunched Ion Beam Optics at CERN–ISOLDE's Offline 2 Separator

Yuval Rosen[†‡], Alexander Schmidt[‡]

[†] *Technion - Israel Institute of Technology, Haifa, Israel*

[‡] *European Organization for Nuclear Research (CERN), Geneva, Switzerland*

September, 2025

Abstract

This work takes place at the Offline 2 laboratory – part of the CERN-ISOLDE Offline facilities – a suite of installations required to perform essential quality control on target and ion source units before their operation at CERN-ISOLDE [1]. Presented are the investigation and design efforts made as part of the latest developments, through SIMION simulations, providing broad understanding of the ion extraction from the Radio Frequency Quadrupole (RFQ), following a drift tube modeling and further lensing and steering capabilities that were simulated and characterized for maximal transmission downstream. The results establish a solid understanding of the system behavior, together with proposed designs of the drift tube and steering Einzel lens prepared for implementation.

Contents

1 Introduction

1.1 Ion Optics

Ion extraction and beam navigation are fundamental topics that must be well studied and then implemented to ensure high transmission and sufficient measurements. Ion beam shaping – bunching, focusing, and steering – relies on the interaction of ion charge with electromagnetic (EM) fields and is commonly referred to as ion optics. However, shaping the spatial EM field profile – analogous to the refractive index in geometric optics – is not as straightforward, because no medium directly participates in the interaction. Instead, electrodes and magnets are designed to shape the desired EM profile indirectly. In this context, two elementary equations govern the beam dynamics – the Lorentz force law and Laplace's equation respectively,

$$\boldsymbol{F} = q\boldsymbol{E} + q\boldsymbol{v} \times \boldsymbol{B} \quad , \quad \nabla^2 \phi = 0$$

Intricate designs often lack an analytic solution relating beam shaping to the applied voltages or currents, so simulations are the primary means to examine beam behavior: solve Laplace's equation numerically, compute forces from the resulting potential gradients, and track particle trajectories in time.

1.2 Simulation – SIMION software

SIMION is a software package for simulating ion optics. It models ion trajectories by solving Laplace's equation on a discretized grid, generating potential arrays (PA's) that define the fields in space. The electric field $\boldsymbol{E} = -\boldsymbol{\nabla}\phi$ is then applied in the Lorentz force law to compute ion motion step by step. This numerical approach relies on iterative averaging, historically described by the rubber-sheet and resistance-paper models. In the *rubber-sheet model*, the potential field is visualized as a stretched surface where electrode voltages set the "heights," and ions behave like marbles rolling along the contours. In the *resistance-paper model*, shaped electrodes are pressed against a sheet of uniform resistivity, voltages are applied, and the resulting potential distribution is measured with a probe. SIMION employs the resistance-paper analogy in its calculations, by iterating over the averaging process of the N cartesian nearest neighbors (n.n.):

$$\phi^{(n+1)}_{i,j,k} = \frac{1}{N} \sum_{(\ell,m,n)\,\in\, n.n.} \phi^{(n)}_{\ell,m,n} = \frac{1}{N}\left(\phi^{(n)}_{i+1,j,k} + \phi^{(n)}_{i-1,j,k} + \phi^{(n)}_{i,j+1,k} + \phi^{(n)}_{i,j-1,k} + \phi^{(n)}_{i,j,k+1} + \phi^{(n)}_{i,j,k-1}\right)$$

SIMION also provides a potential-energy view based on the rubber-sheet model, which is conceptually more intuitive, but less practical for numerical implementation.

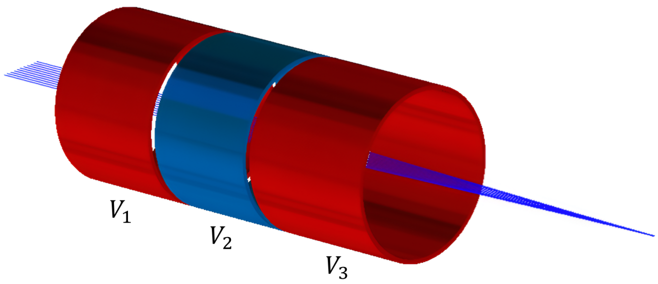

Figure 1: Einzel lens model and ion trajectories.

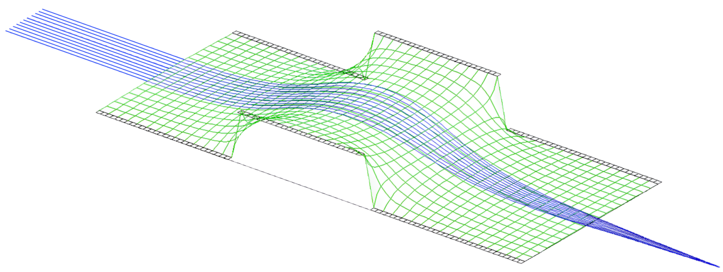

Figure 2: Einzel lens in PE view.

Through this framework, SIMION serves as a practical tool for designing and optimizing a wide range of ion optical elements, offering clear insight into beam transport and shaping even for complex configurations.

1.3 System Overview

The ion beam starts at the **Frontend**, where the target and ion source are kept at high ∼ 30 kV, setting the beam energy. Right after extraction through a grounded electrode, the beam goes into a quadrupole triplet and steerers that shape and align it.

It then enters the **90° dipole magnet** mass separator. The bending magnet filters ions according to their mass-to-charge ratio and focuses the selected beam into a slit at the focal plane. The magnet edges also provide vertical focusing. Diagnostic devices (wire scanners, Faraday cups) are located at these focal points to monitor the beam profile and intensity.

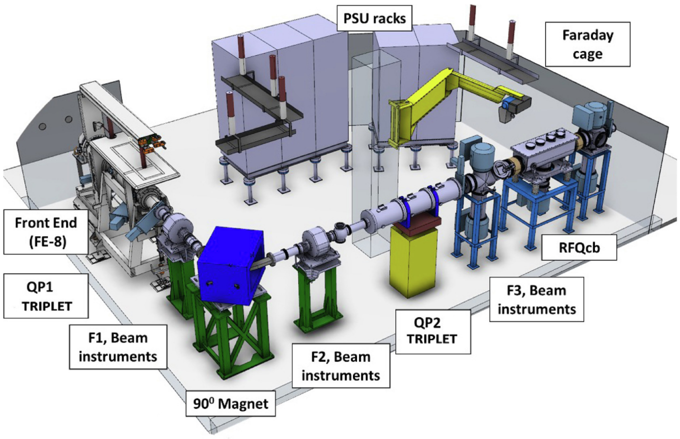

Figure 3: Offline 2 facility system setup [1].

Following mass separation, a second quadrupole triplet focuses the transmitted ions into the **Radio Frequency cooler-buncher (RFQcb)**. Inside the RFQ, the beam is decelerated to rest and guided through a helium buffer gas, where the combined axial DC and quadrupole RF fields reduce the transverse emittance and energy spread while enabling bunching. The resulting cooled and bunched ion packets are re-accelerated and directed downstream – this stage marks the starting point of the present work.

1.4 Motivation

After the ions are extracted from the RFQ, they are expected to travel through two additional instruments: the **Wien filter**, which provides further mass selection for molecular studies, followed by the **Optical Region**, where the ions interact with finely tuned laser light and emit fluorescence collected in this area. Both instruments introduce very narrow apertures and are located about 1.4 m downstream of the RFQ, so that focusing and steering must be implemented. Between them lies a 0.2 m drift region with no space available for additional refocusing in front the optical region aperture. This introduces the first problem — the need for single focusing with two focal points to pass through.

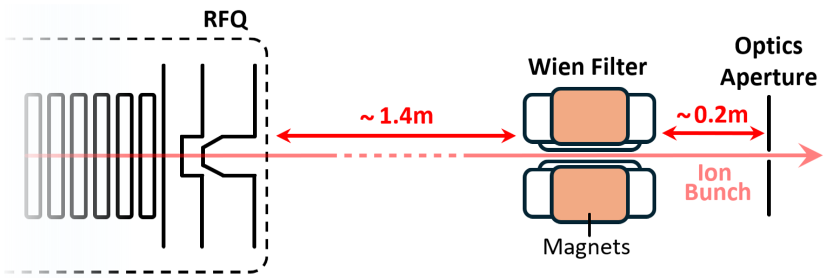

Figure 4: End of beamline – initial draft.

The second problem is that the ions are trapped within ∼ 30 kV electrodes, though low–energy beams are desired as well for other purposes. The simplest solution for the required energy modulation to be analyzed is a pulse drift tube.

2 Analysis & Results

In Fig. 5 a diagram is presented of the final configuration that was selected after the simulation optimization efforts described below.

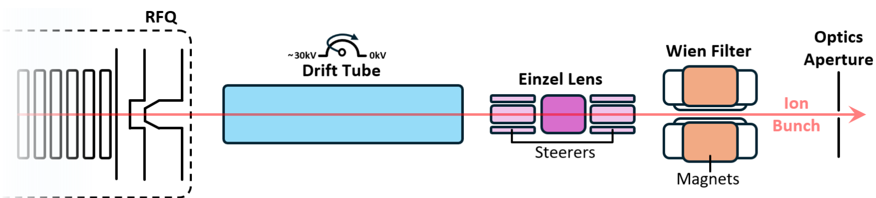

Figure 5: End of beamline – optimized instrumentation.

These efforts resulted in efficient extraction combined with a voltage–switching tube to lower the beam energy, along with a single double–steering Einzel lens capable of high performance both in the high 30 keV beam case (with ∼14 kV) and in the low 5 keV beam region (∼2 kV). The configuration achieved transmission efficiencies of up to 60% for the high–energy bunches while rising to 80% for low–energy case, when not considering extraction losses, which are difficult to simulate reliably and in practice unavoidable. All simulations were using Ba^+ ions.

2.1 Focusing Solution & Extraction Optimization

Facing the dual–focal point issue, many attempts were made to increase the transmission downstream, as the beam tended to spread out quickly after extraction in the first stages (handled later). These attempts were guided by the following considerations:

Engineering limitations: Space availability, mounting options, electrode spacing to prevent sparking (following the ∼1 MeV/m electric field safety upper limit rule of thumb), and the requirements of high– and low–voltage feedthrough flanges.

Resource friendly: For future implementation, the design must perform up to a standard that satisfies its purpose (desired transmission) while justifying the associated budget.

Validated physical basis: The gap between simulation and reality must be acknowledged, especially in the context of simulation limitations. SIMION is known as a simplified yet reliable framework, but at the cost of omitting certain physics. Understanding the criticality of these omissions is essential to assess the credibility of the simulation results. This applies to both macroscopic effects, such as space charge, and microscopic effects, such as interactions with edge fields.

Three models yielded far better transmission than the other attempts, while differing in how they addressed the considerations above. The first two, (A) and (B) in Fig. 6, acted as **telescopes**: they accepted a wide beam (in angle and width) and produced a narrower one with smaller angular spread, capable of holding both focal points with high precision. The third, (C), was a simple optimized Einzel lens.

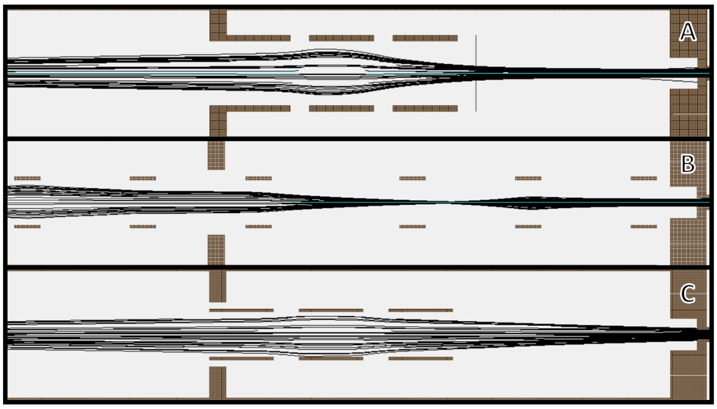

Figure 6: Proposed focusing models: (A) uses an Einzel lens and a lattice, (B) uses two Einzel lenses, and (C) uses a single Einzel lens.

Model (A) uses an Einzel to focus the beam, then expands it slightly before the focal point using a lattice, effectively a penetrable electrode – the voltage scan results appear in Fig. 7. However, the cost of producing such a lattice and the uncertain losses in simulation made it quite unappealing. Placing an electrode within the beam cross section has not been used to *enhance* transmission before; the only case found was in ion thrusters, and although they produced impressive thrust power, lattices were applied for ion extraction rather than focusing [2]. Simulating realistic interaction with the lattice was also impossible with SIMION, and in addition, the model didn't seem to hold for high energy beams (transmission dropped to ∼40%). Thus overall, this approach was not considered attractive.

Models (B) and (C) were then left to compete. Both handled high– and low–voltage cases similarly within each energy setting; however, the telescope consistently outperformed the Einzel at both energies.

The values below are shown for the high 30 keV beam (the low–energy case exhibited essentially the same relative advantage): up to 100% vs. 40% for the low–emittance beam, and 40% vs. 20% for the high–emittance case. Emittance was set by widening the angular distribution at entry, achieved by varying the ions' initial positions within the extraction region – moving the ions farther from the extraction aperture reduced emittance, since the solid angle connecting the start position to the aperture is smaller.

In the telescope, the first Einzel lens' outer plates were scanned against the middle plate of the second Einzel, while the first lens' middle plate was held constant at −20 kV. This produced effective focusing at entry via the potential gradient between the grounded housing and the first plate, followed by a strong negative focusing from the gradients between the positively biased outer plates and the middle plate of the first Einzel. This scheme enabled finer focusing than the traditional positive–bias focusing of the inner plate. The comparison of results appears in Fig. 8. The required $\sim$ 27 kV are beyond the available SHV 20 kV limit, which already makes the telescope implementation more difficult.

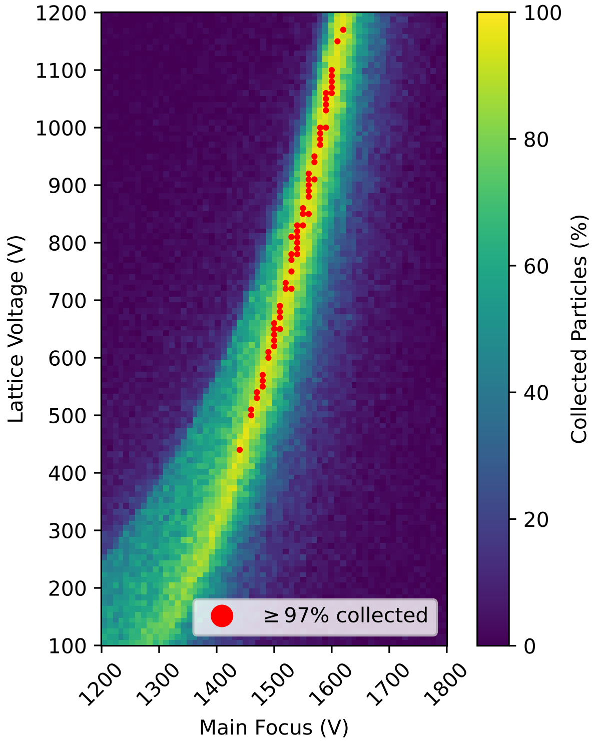

Figure 7: Einzel lens and lattice voltage scan for 5keV beam - transmission heatmap downstream (no losses on lattice).

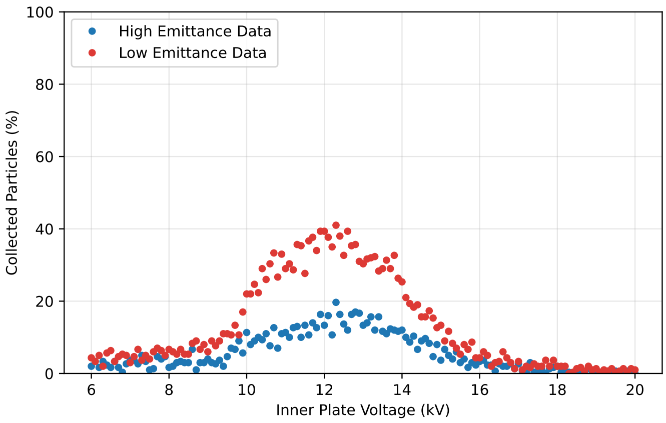

(a) Einzel lens voltage scan.

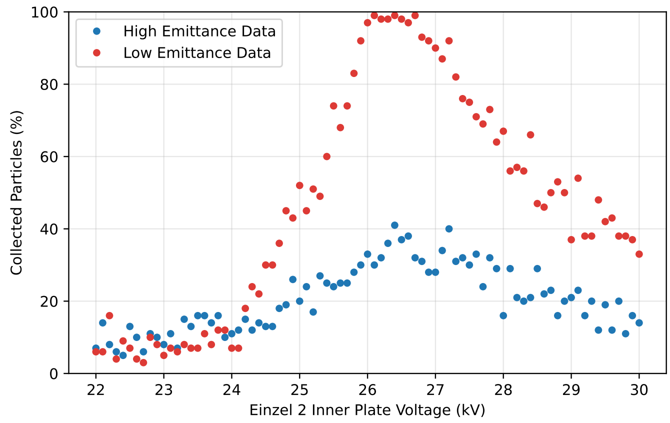

(b) Telescope voltage scan — sliced from 2D scan at 13.4 kV on Einzel 1 outer plates.

Figure 8: Transmission comparison at high energy for high/low emittance.

At the next stage, the acceleration plates at the end of the RFQ were scanned for optimal extraction, with the drift tube held at a fixed voltage. With 6 kV power supplies attached to the conical and rectangular electrodes (see Fig. 4), the full parameter space of these two electrodes was scanned for each chosen drift–tube voltage (i.e., the desired output beam energy). For example, setting the drift tube to 25 kV ideally yields a $30 - 25 = 5$ keV beam. The results appear in Fig. 9.

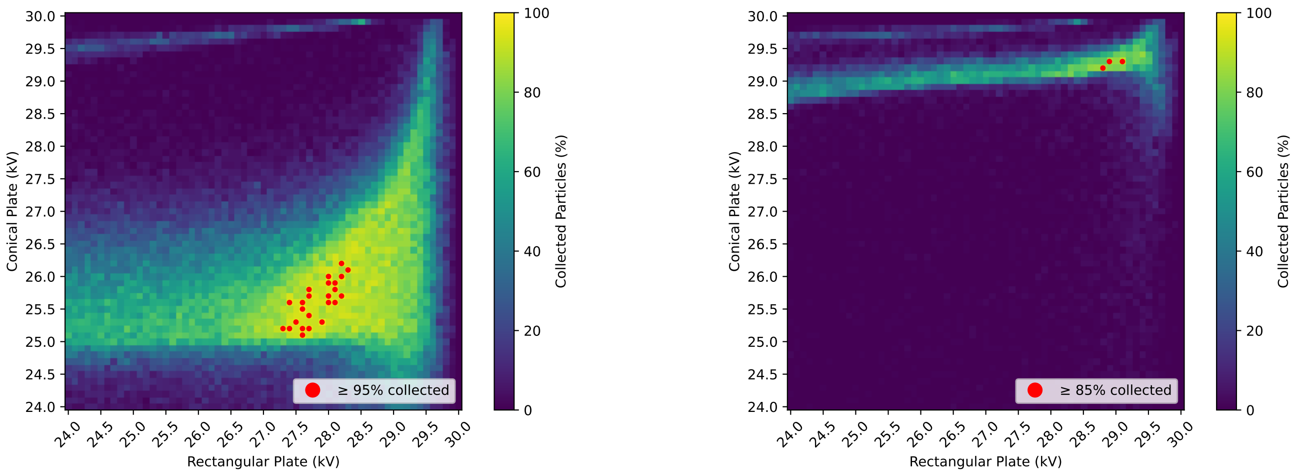

(a) 30 keV beam extraction.

(b) 5 keV beam extraction.

Figure 9: Acceleration plates voltage scans – captured right before focusing region.

Two pairs of voltages were selected, the results are summarized in Tab. 1. For the high–energy case, a broad region of high transmission was observed and tested, with no significant variation in the post–extraction angular distribution across this range. These operating points were then used to rescan the focusing quality, as shown in Fig. 10.

Beam energy	Voltages applied	Avg. trans.
5 keV	(29.1 kV, 29.3 kV)	$81.45 \pm 0.33\%$
30 keV	(27.6 kV, 25.5 kV)	$95.07 \pm 0.21\%$

Table 1: Selected extraction voltages and transmission, averaged over 30 runs of 10,000 ions, captured upon entry of the focusing region.

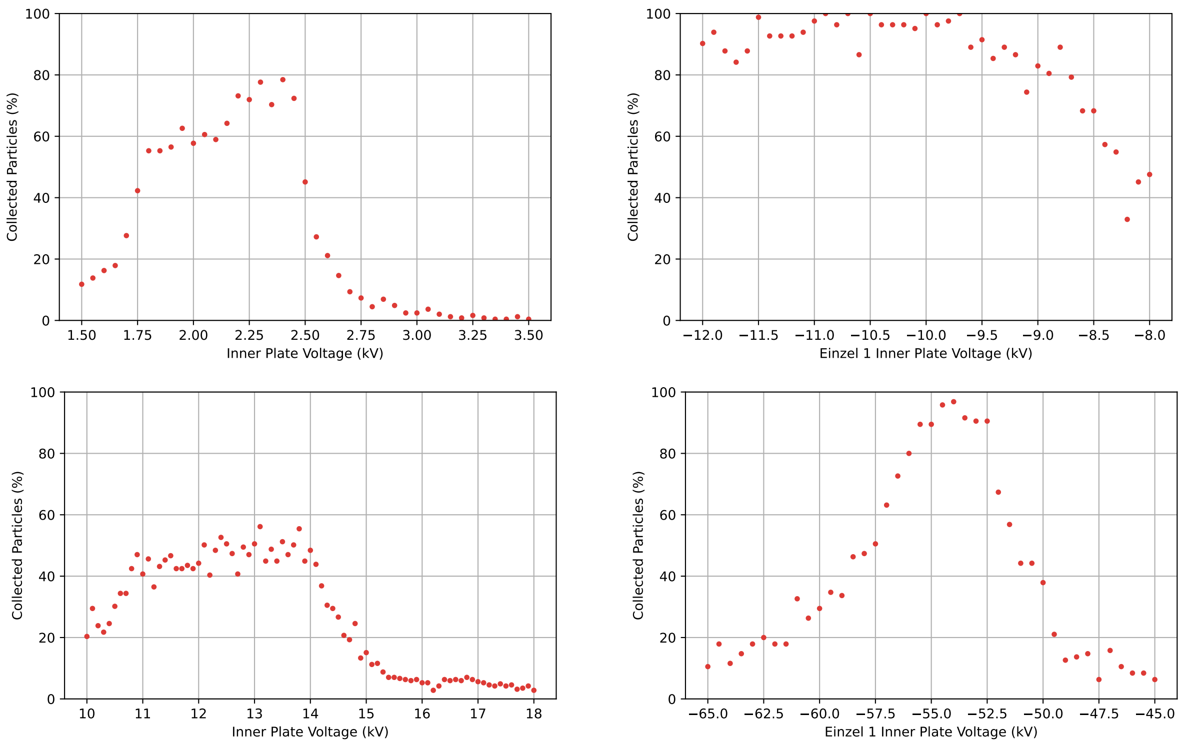

(a) Einzel lens voltage scan.

(b) Telescope voltage scan – sliced from 2D scan.

Figure 10: Upper row – low–energy scan; bottom row – high–energy scan (telescope data sliced at 4.1 kV and 26.5 kV on Einzel 2, respectively).

Note that at this stage the telescope employed simple double–Einzel focusing: the outer plates of the first Einzel were grounded, since the simulated gradient between the vacuum housing and the outer plates was unreliable, and there was insufficient space for four high–voltage feedthroughs. Thus, the first Einzel operated with extreme high voltage negative focusing while its outer plates remained grounded.

The extraction–optimized results in Fig. 10 reduced the efficiency gap between the telescope and the single Einzel, with the latter showing notably higher performance than before. Considering cost and practicality, the telescope lagged far enough behind, such that its great performance did not justify its implementation. Consequently, the single Einzel configuration was adopted, accepting some transmission losses, as the achieved efficiency remains adequate for the measurement requirements.

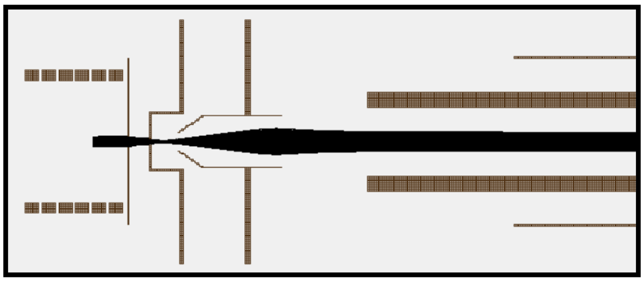

Figure 11: Extraction telescoped 5 keV beam.

A nice aspect, even though the telescope configuration was dropped after intensive work, is that its spirit still lived on in the system — the optimized extraction plates in fact telescope the beam as it emerges, as seen in Fig. 11.

2.2 Pulse Drift Tube

The Pulse Drift Tube is a simple cylinder acting as a Faraday cage for the bunch. It reduces the beam energy to the desired value as follows: the bunch enters the tube, which is held at a voltage lower than the extraction plates by the desired acceleration (directly setting the beam energy).
Once the bunch was entirely inside, the tube voltage was switched to ground (or several kV if chosen), so the bunch experienced no change. Upon exit, the bunch carried an energy equal to the initial voltage *difference* between the tube and the 30 kV trapping electrodes, rather than the default 30 keV imposed by these electrodes. The entire process occurs in less than 10 µs, and the bunch length and dynamics and interaction with the drift tube had to be carefully studied to avoid truncation and transmission loss. The following analysis was performed with voltages of 2.4 kV and 14 kV applied to the Einzel lens middle plate for beam energies of 5 keV and 30 keV, respectively.

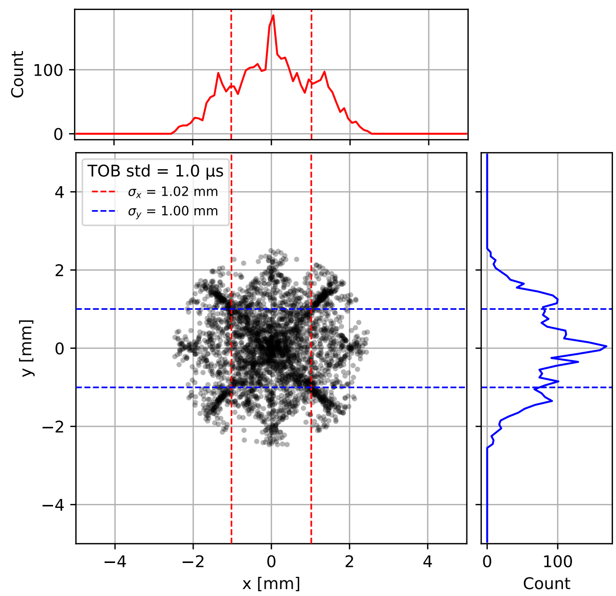

Figure 12: 5000 ions beam cross section statistics captured downstream – ion average energy of 4990 eV was captured at 82% transmission (extraction losses omitted).

2.2.1 TOB Measurements & Switching Time

The bunch length is commonly defined in temporal rather than spatial terms, since time is conserved across different velocities along the trajectory. Accordingly, ions were generated within a circular cross section at the center of the trap potential well and released with a Gaussian-distributed **Time of Birth** (TOB). The bunch length must also be well defined inside the tube to ensure it fits entirely within it.

The first step was to examine the bunch behavior and shape downstream through cross-section snapshots and longitudinal reconstructions, as shown in Figs. 12, 13, and 14, using a TOB standard deviation of 1 µs sample.

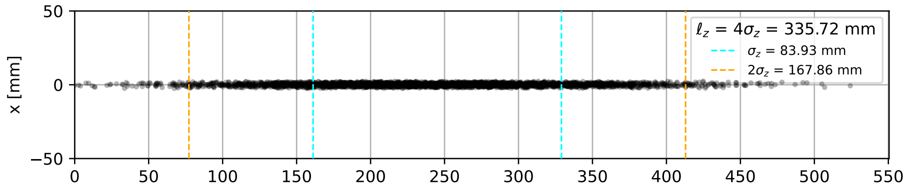

Figure 13: Reconstructed beam by ion velocity and TOF.

The common definition for the temporal bunch length follows a total of 4 STD's of the captured ions **Time Of Flight** (TOF). This truncates only about 5% of the bunch, which is appropriate when considering wandering ions that exceed the bunch defined area, as presented in Fig. 13. Also, the bunch TOB statistics agreed with the TOF analysis, presenting consistent temporal STD's at good precision. This consistency along with transmission rate and average energy were the main indicators for appropriate switching.

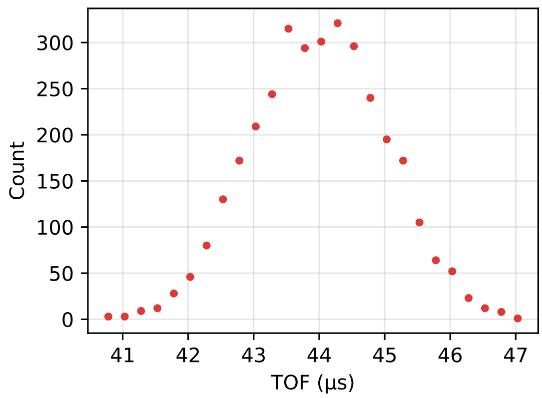

Figure 14: Ion TOF binned histogram downstream of 1 µs TOB STD bunch – calculated TOF STD through Guassian fit: 1.041 ± 0.02 µs.

The final tube design was 600 mm long, and 10 mm thick, with an inner radius of 20 mm and outer of 30 mm. The 5 keV beam velocity is:

$$v = \sqrt{\frac{2E}{m_{\mathrm{Ba}}}} = \sqrt{\frac{2 \times 5 \times 10^3 \times 1.6 \times 10^{-19}}{138 \times (6.022 \times 10^{23})^{-1} \times 10^{-3}}} \approx 83.56\,\frac{\mathrm{mm}}{\mathrm{\mu s}}$$

Thus the temporal length of the tube was $600/83.56 \approx 7.18$ µs, and the equivalent bunch length followed $7.18/4 \approx 1.8$ µs of STD. The potential was probed along the beam axis and off-axis, as seen in Fig. 15. During switching, both ends were affected – ~ 20 mm from the entrance and ~ 30 mm from the exit. These effects, together with the maximal compatible bunch length, were studied further by scanning the switching time for different bunches, as shown for two examples in Fig. 16.

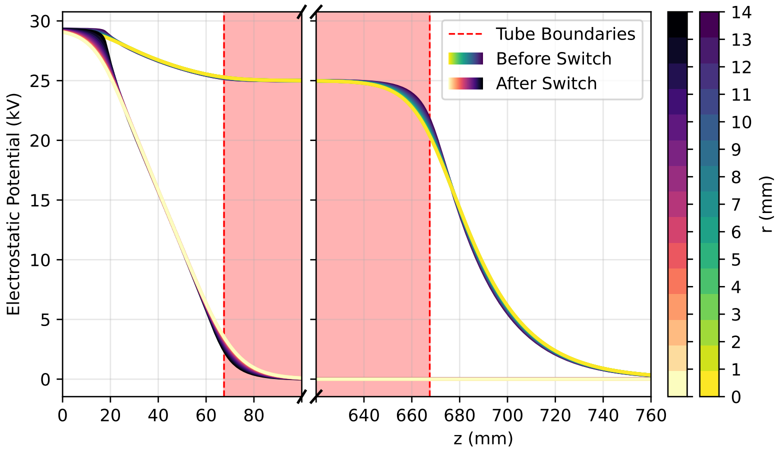

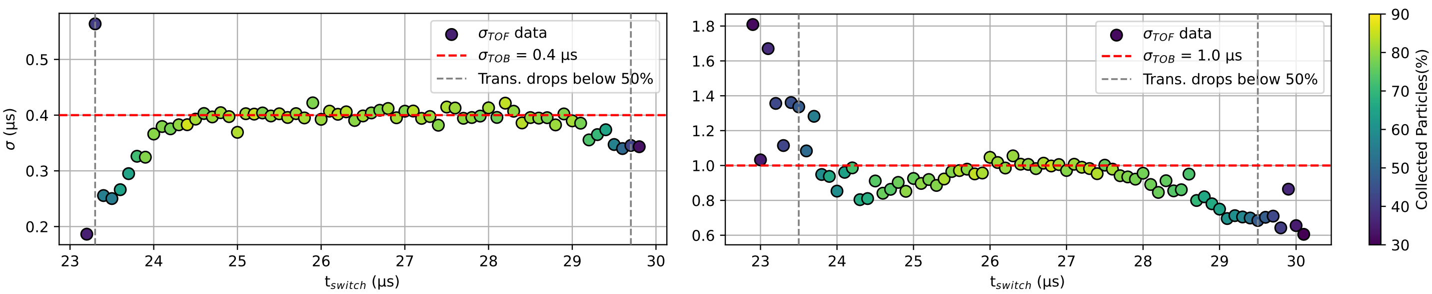

(a) $\sigma_{\mathrm{TOB}} = 0.4$ µs bunch.

(b) $\sigma_{\mathrm{TOB}} = 1$ µs bunch.

Figure 16: Switching time scan results comparison for different bunch lengths (omitting extraction losses).

The parasite edge potential gradients gave certain ions an additional acceleration: those in the entrance gap or near the tube exit gain extra energy per early or late switching respectively. Note that the data in these specific figures was not derived from Gaussian fits – the reason for this and further analysis will be discussed later†.

A comprehensive switching time scan is shown in Fig. 17. As the TOB standard deviation increased, both the overall and peak transmission decreased, and the interval of efficient switching narrowed. This reflected the growing influence of edge gradients on the bunch, which eventually extended beyond the tube length at higher TOB STDs. This effect seemed to lower the average TOF STD, since edge ions were accelerated, detaching from the bunch, thus narrowing the TOF distribution. This is analyzed in Fig. 18.

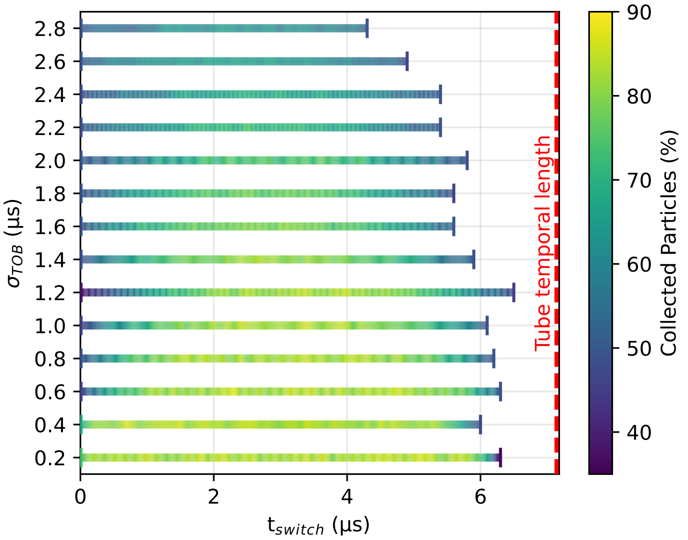

Figure 17: Switch scan for all compatible bunch lengths, left aligned for full interval comparison. Continuous gradient added to interpolate between measured data points.

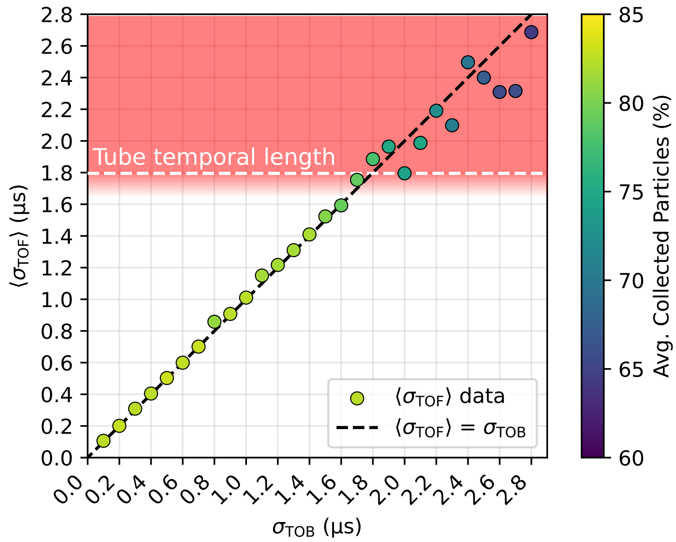

Figure 18: Average TOF STD during the switch scan, calculated from data points above 80% of maximal transmission across TOB STDs. The red gradient marks the tube boundary-affected region.

As transmission dropped and edge–accelerated ions dominate, bunch statistics lost consistency. This is evident in Fig. 19, where bunch edges truncated: back–end ions (higher TOF) were lost, and the Gaussian profile was cut off near the tube temporal length of ∼ 7.18 µs (plotted for optimized switching time).

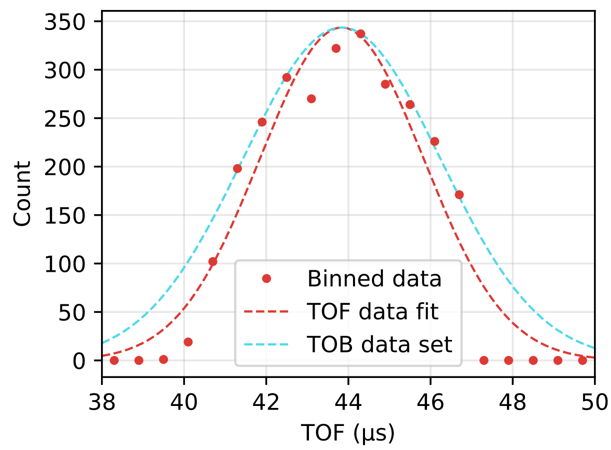

Figure 19: Ion TOF binned histogram downstream of 2.4 µs TOB STD bunch – calculated TOF STD through Guassian fit: 2.332 ± 0.078 µs. Avg. energy – 5036 eV with 68% transmission (extraction losses omitted).

2.2.2 Misalignments & Steering

The next step toward implementation was to investigate the effect of installation misalignments. Given the significant potential gradients involved, such effects cannot be neglected. The practical question was whether adequate misalignments can be compensated through appropriate electrode steering, rather than by drilling specialized knobs into the vacuum housing to enable external tube alignment — a solution that is far less appealing in terms of cost and fabrication.

For the 5 keV beam, the misalignment produced a greater deviation, as the ions spent more time traveling through the gradients. Beam statistics were recorded immediately after the drift tube in order to capture the misalignment effect. Fig. 20 presents the case of a 0.5° off-axis tube alignment.

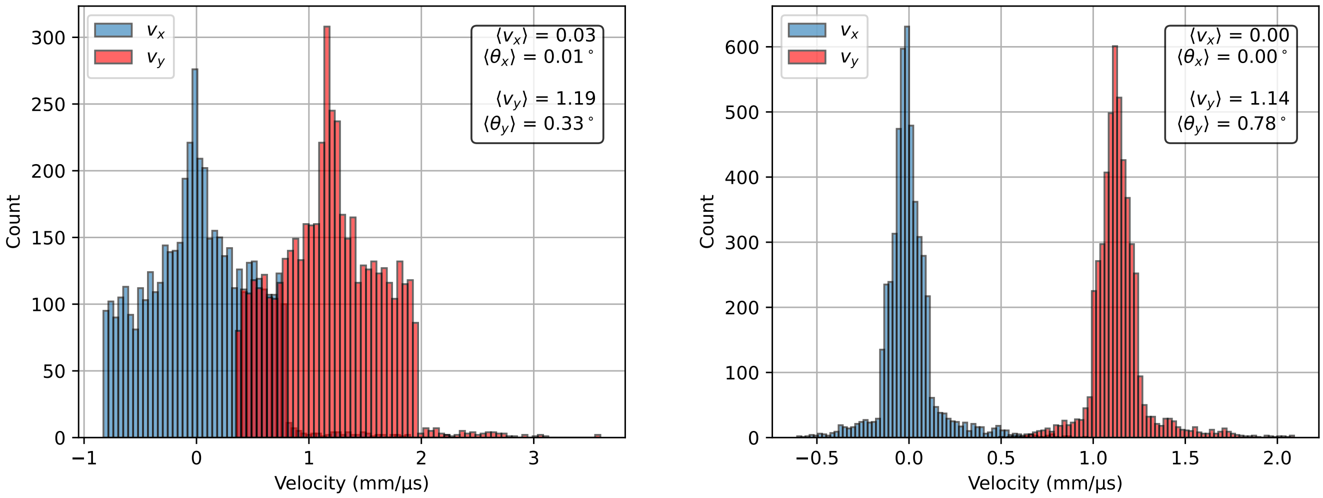

(a) 30 keV beam. (b) 5 keV beam.

Figure 20: 0.5° off-axis drift tube misalignment – beam velocity statistics

Figure 21: 0.5° misalignment acceptance of 5 keV beam at focusing region - single (A) vs. double (B) steerer cases. Steering electrodes marked in pink.

As a result, a single steerer implemented in the Einzel lens was not sufficient to recover transmission in the low-energy case. An alternative solution with a double–steering implementation was therefore considered, as shown in Fig. 23. Each steerer consisted of a cylindrical electrode divided into four quadrants, with voltages applied in a symmetric manner. For example, a "positive" steering action (in the $+y$ direction) was achieved by applying a positive voltage $+V$ to the lower electrode and a negative voltage $-V$ to the upper electrode. An asymmetric polarization configuration, in contrast, would have introduced an undesired quadrupole effect, focusing the beam along one axis while simultaneously defocusing it along the transverse axis.

Both steerers were cross-scanned to test the model performance, as shown in Fig. 22 for example. The voltage sign convention is defined as mentioned above. In addition, off-center misalignments of 1 mm and even 2 mm were tested, for which the double steering model not only recovered the former transmission, but in fact increased it beyond the original value. This result was somewhat surprising, as it suggests that misaligning the tube and then correcting with the steerers could yield higher transmission. The scan results were averaged by columns and fitted with linear regression, as all scans exhibited linear behavior with a high $R^2 \approx 0.99$. The results are presented in Fig. 23, with the 2 mm case omitted for clarity of visualization.

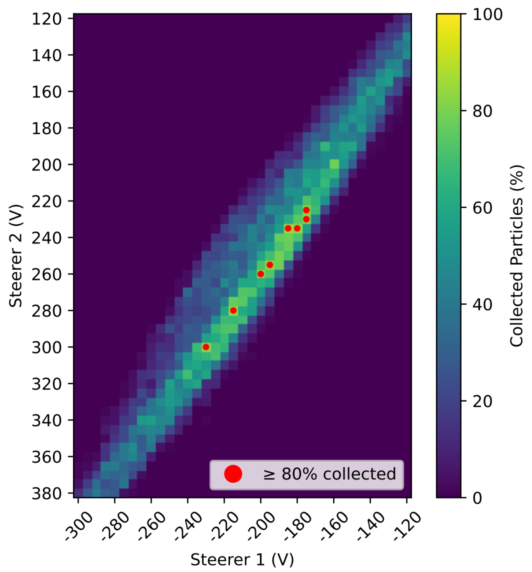

Figure 22: 0.5° off-axis misalignment, 5 keV beam double steerer voltage scan.

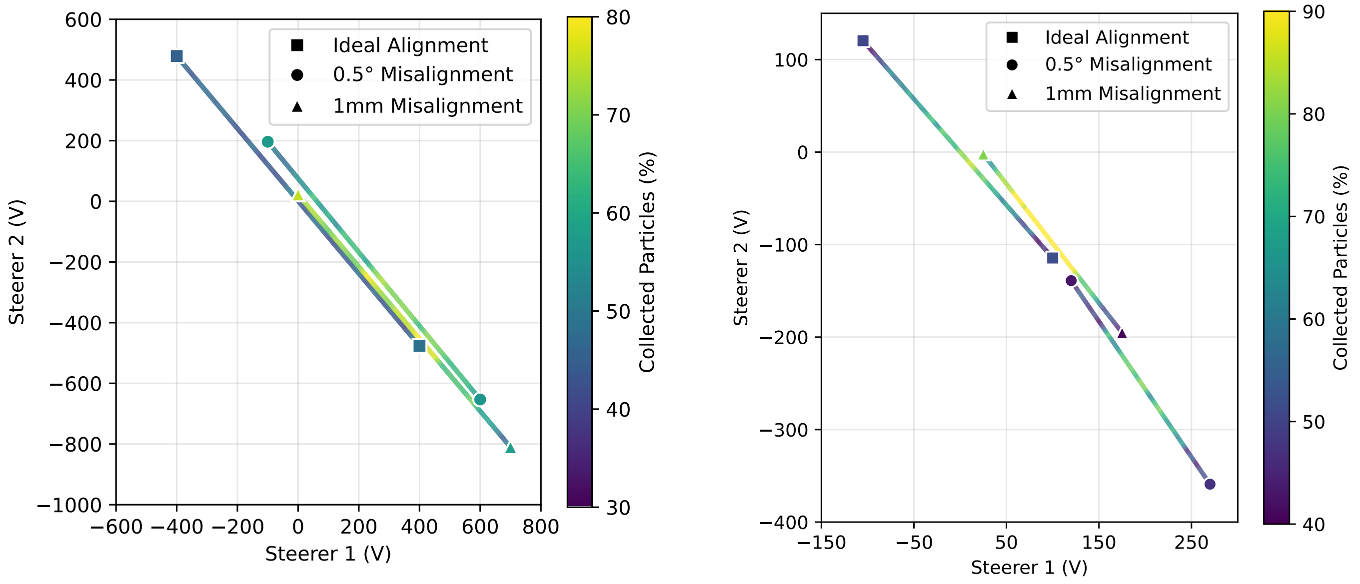

(a) 30 keV beam. (b) 5 keV beam.

Figure 23: Double–steerer voltage scan comparison for tube misalignment.

It is also important to note that the focusing voltage applied to the middle Einzel was reduced to 90% of its previous value for further optimization, since the steerers interacted with the focusing field.

3 Discussion & Implementation

Presented above were the conditions for producing high–transmission bunching up to a simulation standard, among which are efficient extraction, well–timed voltage switching, precise focusing and steering, by this order downstream. For implementation purposes, CAD models were assembled accordingly towards fabrication – the models appear below, along with the proposed assembly:

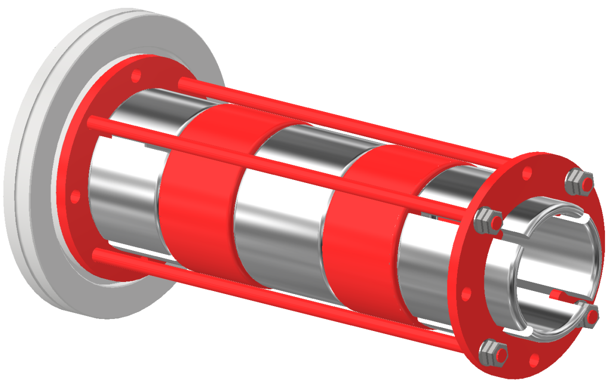

Figure 24: Double–steerer Einzel lens model.

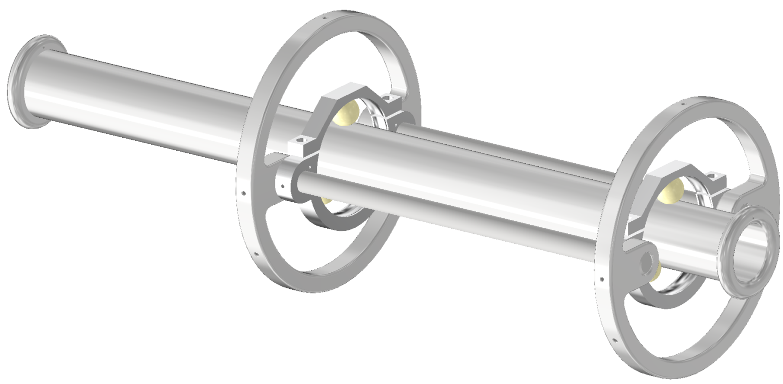

Figure 25: Drift tube model.

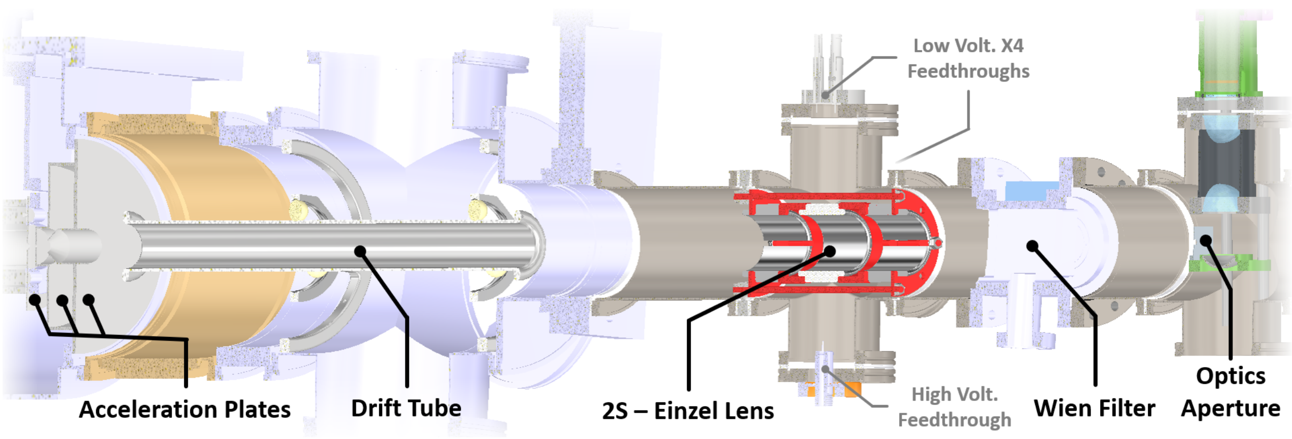

Figure 26: End of beamline assembly – full setup model

Unlike in simulation, the voltage does not appear instantaneously everywhere, but propagates through the conductor at a finite velocity determined by EM wave propagation in the material, at some given relaxation time determined by the switcher. Thus, the voltage at a point along the tube can be described as:

$$V(t) = V_0 \, e^{-\frac{t-t_0}{\tau}} \quad , \quad t_0 = \frac{\ell}{v_p}$$

where ℓ is the distance from the feed connection to the point of interest, and v_p is the propagation velocity of the voltage signal in the conductor (of order c in vacuum, reduced by the dielectric environment). The characteristic time constant τ reflects that the drift tube acts as a capacitance C, while the cables and switching pulser introduce an effective resistance R, so together the system settles exponentially with the typical response of an RC circuit once the signal front has arrived. Since typically $t_0 \ll \tau$, the switching device's specifics will determine the switching rate τ.

Aiming for $\sigma \sim 1$–$2\,\mu s$ bunching, an estimate interval of 1 µs can be used to gain at least 70% transmission with the current setup. Therefore having $\tau \sim 0.2\ \mu s = 200\,ns$ follows a safe threshold for switching:

$$V_{\text{final}} \approx 25 \times 10^3 \times e^{-\frac{1}{0.2}} \approx 170\,V$$

This leads to up to $\sim \frac{170}{5000} \approx 4\%$ deviation in energy from the desired 5 keV beam.

There are several technologies that implement high-voltage switching, such as thyratrons, spark gaps, and modern solid-state MOSFET stacks [3]. The latter, for example, provide solutions for $\sim$ 30 kV switching with rise times below 200 ns, making the procedure above feasible with consistent with both simulation standards and realistic experimental parameters.

σ_{bunch} (µs)	>50% (µs)	>60% (µs)	>70% (µs)	>80% (µs)
0.2	4.40	4.35	4.27	4.07
0.4	5.26	5.09	4.96	4.69
0.6	3.98	3.82	3.61	3.21
0.8	3.77	3.51	3.30	2.45
1.0	2.66	2.42	1.92	0.95
1.2	2.40	1.96	1.62	0.66
1.4	3.18	2.61	2.07	1.02
1.6	2.50	2.13	1.45	0.05
1.8	3.03	2.42	1.75	–
2.0	2.16	1.72	0.71	–
2.2	2.87	2.13	1.12	–
2.4	2.86	2.11	0.51	–
2.6	2.01	1.25	–	–
2.8	2.10	1.63	–	–

Table 2: Maximal switching time intervals for final transmission thresholds downstream (omitting extraction losses). Captured from last drop below each threshold, using the interpolated data.

As seen in Tab. 2, while for each bunch STD the transmission increases with decreasing switching time intervals, some inconsistencies appear among different bunch STDs (since higher bunch STDs should generally yield lower transmission rates), as seen among 0.2 µs to 0.4 µs, as well as 1.2 µs to 1.4 µs. These inconsistencies could be reduced by sampling a larger number of ions with higher scan resolution, though the present simulation results provide a general overview for the temporal analysis required to implement an adequate switching mechanism.

4 Conclusions & Further Investigation

The present work established a comprehensive simulation framework for the extraction, focusing, and steering of ion beams downstream of the RFQ. The simulations demonstrated that optimized extraction voltages on the first acceleration plates provide stable operating points with high transmission. An important finding was that the optimized extraction geometry effectively telescopes the beam at its emergence, reducing divergence and improving matching into the focusing region.

With regard to focusing, although the telescope models consistently achieved superior transmission in simulation, their added complexity, cost, and fabrication constraints made them less attractive. The optimized single—Einzel lens, combined with efficient extraction, provided transmission rates up to 60% for high–energy beams and 80% for the low–energy ones, which is sufficient for the measurement requirements while offering a design that is simpler and more practical to implement.

The drift tube was designed and characterized as a 600 mm long cylinder, enabling voltage switching to reduce the beam energy once the bunch is fully contained. The analysis showed that bunches with σ_{bunch} around 1–2 µs can be switched with more than 70% transmission if the effective switching interval is kept within ∼1 µs. Edge effects at the entrance and exit of the tube were identified as the main source of transmission loss, producing different distortions depending on whether switching occurred too early or too late. Nevertheless, the proposed design offers a workable solution, provided that realistic switching times of order 200 ns can be achieved experimentally with appropriate pulser technology.

The steering analysis confirmed that practical misalignments are not fatal to transmission. Misalignments of up to 0.5° or several millimeters could be fully compensated by implementing a double–steerer Einzel configuration, and in some cases even led to enhanced transmission. This robustness increases confidence that the system will remain functional under realistic installation tolerances.

Although the present results provide a strong foundation for implementation, several aspects call for further investigation. Wider and finer scans of the extraction plate voltages could help ensure reproducibility under slight mechanical variations. The switching study, while conclusive in general trends, would benefit from larger ion statistics and finer resolution to remove inconsistencies between certain bunch lengths. It could also be beneficial to include realistic switching dynamics in future simulations, incorporating RC time constants and the finite propagation of the applied voltage along the conductor.

In conclusion, the optimized extraction scheme, the single–Einzel focusing lens with double—steering capability, and the drift tube switching method together form a feasible and efficient solution for ion beam transport. With the outlined refinements and experimental validation, this design is expected to provide reliable performance under operational conditions.

5 Appendix

5.1 Bunch Data Analysis & TOF Statistics Processing

In both early and late switching cases the beam is truncated, and the calculated STD gradually decreases once the optimal switching interval is exceeded. However, a sudden rise appears for early switching (seen in Fig. 16b), as the potential gradient spreads the bunch by imparting different velocities to ions according to their longitudinal position – leading to broader velocity distributions in the early switching cases. For example, examining early 23.5 µs and late 29.5 µs switching times for $\sigma_{\text{TOB}} = 1$ µs as shown in Fig. 16b, a longitudinal velocity STD, σ_{v_z}, was measured at 9.8 mm/µs and 0.5 mm/µs respectively, before masking the data by 5 TOF STDs. After masking, 0.7 mm/µs and 0.3 mm/µs were obtained. This reflects the presence of a minor group of highly accelerated on-axis ions that reached downstream together with a moderately accelerated group driven by the edge gradients. This mask was applied in all data analysis.

The reason for this asymmetry is conjectured to lie either in the differing de-focusing effects occurring in the switched gradients at the tube's entry and exit, or in the bunch length in both cases, since the bunch stretches within the entry gap while it is already elongated upon exit.

An interesting question was whether to calculate the TOF standard deviation directly as

$$\sigma_{\text{TOF}} = \sqrt{\frac{1}{N}\sum_{i=1}^{N}(t_i - \bar{t})^2}, \quad \bar{t} = \frac{1}{N}\sum_{i=1}^{N} t_i$$

or by fitting to a Gaussian profile and extracting its width. This stems from the understanding that the Gaussian model does not hold for certain measurements, in which a significant fraction of the ions exceed the tube's optimal switching length. Therefore, it was decided to continue with the measurements corresponding to above 80% of maximal transmission for each σ_{TOB}, as in Fig. 18. Within this region, the data showed quite consistent statistics for narrow bunch lengths, as seen for example in Fig. 27. This supports the credibility of the presented analysis. In Tab. 3, a summary of all datasets is presented. Some of these experienced poor statistics, which may require a more adaptive masking method than the fixed 80% transmission threshold, or one independent of transmission altogether. Additional finer data scans could also improve the results.

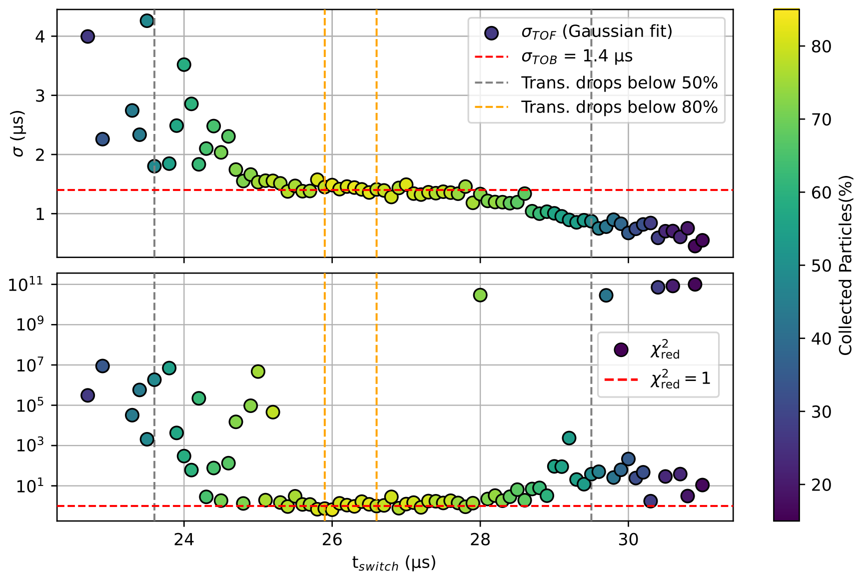

Figure 27: Bunch TOF STD extracted from Gaussian fit — 1.4 µs bunch TOB STD, with reduced chi square for each data set. $\langle\chi^2_{\text{red}}\rangle = 1.08$ over the top 80% of maximal transmission.

σ_{TOB} (µs)	0.2	0.4	0.6	0.8	1.0	1.2	1.4	1.6	1.8	2.0	2.2	2.4	2.6	2.8
$\langle\chi^2_{\text{red}}\rangle$	1.40	1.23	1.41	1.72	1.14	1.24	1.08	1.75	28.93	11.30	2.59	3.01	3.27	4.85
$\sigma(\chi^2_{\text{red}})$	0.58	0.62	0.75	0.47	0.56	0.29	0.32	0.77	27.95	17.88	0.74	2.12	1.49	2.17

Table 3: Average reduced χ^2 and its standard deviation within the top–80% transmission window, for each injected bunch width σ_{TOB}.

References

[1] Maximilian Schuett et al. "Developments at the CERN-ISOLDE Offline 2 mass separator". In: *19th International Conference on Electromagnetic Isotope Separators and Related Topics (EMIS 2022), Daejeon, Korea, 3–7 Oct 2022*. Vol. 541. © 2023–2025 The Authors (CC BY 4.0). Elsevier, 2023, pp. 82–85. DOI: 10.1016/j.nimb.2023.04.053.

[2] Miguel L. San Gregorio et al. "Ion engine grids: Function, main parameters, issues, configurations, geometries, materials and fabrication methods". In: *Chinese Journal of Aeronautics* 31.8 (2018), pp. 1635–1649. DOI: 10.1016/j.cja.2018.06.005.

[3] HV Products GmbH. *Solid State Switches*. Accessed: 2025-08-26. 2025. URL: https://www.hvproducts.de/solid_state_switches.